

Growth of Transition-Metal Cobalt Nanoclusters on 2D Covalent Organic Frameworks

Toyo Kazu Yamada,* Shingo Kanazawa, Keisuke Fukutani, and Satoshi Kera

Cite This: <https://doi.org/10.1021/acs.jpcc.3c07435>

Read Online

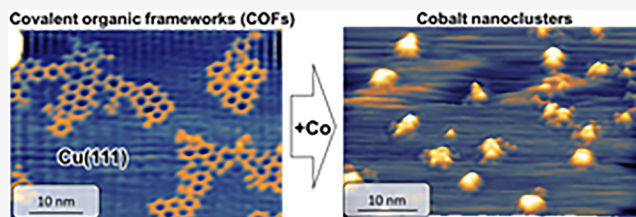
ACCESS |

Metrics & More

Article Recommendations

Supporting Information

ABSTRACT: Two-dimensional (2D) covalent organic frameworks (COFs) fabricated through on-surface synthesis were investigated as a honeycomb nanopore template for the growth of 3d-transition-metal nanoclusters (NCs) with a size of 2 nm on a metallic substrate. The evolution of these NCs and their electronic characteristics were studied employing scanning tunneling microscopy/spectroscopy (STM/STS), angle-resolved ultraviolet photoelectron spectroscopy (ARUPS), and X-ray photoelectron spectroscopy (XPS) under an ultrahigh-vacuum (UHV) condition at room temperature. The 2D COFs were synthesized on Cu(111) substrate utilizing 1,3,5-tris(4-bromophenyl)benzene (TBB) precursors, which engendered a honeycomb nanopore array of approximately 2 nm in size. In contrast to the behavior observed in the Co/Cu(111) system producing triangular-shaped bilayer-stacking nanoclusters measuring 10–20 nm, STM imaging of Co/COFs/Cu(111) revealed the growth of Co NCs of approximately 1.5 nm within a single COF nanopore. This growth occurred without forming a monolayer film beneath the COFs, providing direct evidence that the 2D COFs on Cu(111) can effectively entrap Co atoms within the nanopore, giving rise to Co NCs. Spectroscopy measurements, including STS/UPS/XPS, confirmed the different Co local densities of states for Co NCs and COFs, corroborating the coexistence of Co NCs and COFs on the surface.



1. INTRODUCTION

Among the robust intermolecular interactions, covalent bonding between carbon atoms has attracted notable attention. Recently, this bonding has been harnessed to create covalent organic frameworks (COFs), a remarkable nanostructure that has emerged as a pioneering innovation in the past few decades. COFs serve as nanometer-scale templates, adept at accommodating guest nanomaterials with an exceptionally high packing density. This property holds great promise for various advanced applications, including gas storage and separation,^{1–3} catalysis,^{4–6} drug delivery,^{7–9} photoelectronic devices,^{10–12} and batteries.^{13,14}

A thorough comprehension of the mechanisms by which guest materials become entrapped within COFs, whether through electronic bonding or otherwise, is pivotal for determining the functionality of COF-based applications. Notably, both three-dimensional (3D) COFs, synthesized in solution, and two-dimensional (2D) COFs, prepared on noble-metal surfaces through on-surface synthesis, have been developed.^{15–24} In the case of 2D COFs, precursor molecules are utilized on atomically flat metal substrates, triggering thermal diffusion and chemical reactions that culminate in forming a 2D nanopore network.

Our primary focus lies in discerning whether these 2D COFs possess the capability to capture adsorbed transition-metal atoms within their nanopores, thereby engendering artificial magnetic nanoclusters (NCs) measuring a mere few nanometers in size. Such NCs hold tremendous potential for a broad

spectrum of applications, encompassing quantum dots,^{25,26} quantum bits,^{27,28} spintronics,^{29,30} biomedicine,^{31,32} drug delivery,^{33,34} catalysts,^{35–37} and water purification.³⁸

The utilization of organic compounds to immobilize magnetic atoms on a surface was initially demonstrated on the surface of π -conjugated molecular self-assembled monolayer (SAM) films, such as phthalocyanines or porphyrins.^{39–41} However, a single molecule can only accommodate one atom at its core in this metalation process. Suppose the deposition of transition-metal atoms surpasses the number of organic molecules within the SAM film. In that case, excess 3d atoms push out the molecule and prefer to contact the noble-metal substrate. This results in intercalation, the formation of multiple adcomplexes, and the disruption of the ordered SAM array, ultimately yielding an uncontrolled and disordered surface.^{39,40,42} In essence, SAM films lack the capability to capture dozens to hundreds of magnetic atoms.

In this study, our focus is directed toward the experimental investigations of the initial growth of submonolayer cobalt (Co) on a 2D COFs film prepared on an atomically flat and

Received: November 9, 2023

Revised: December 19, 2023

Accepted: December 20, 2023

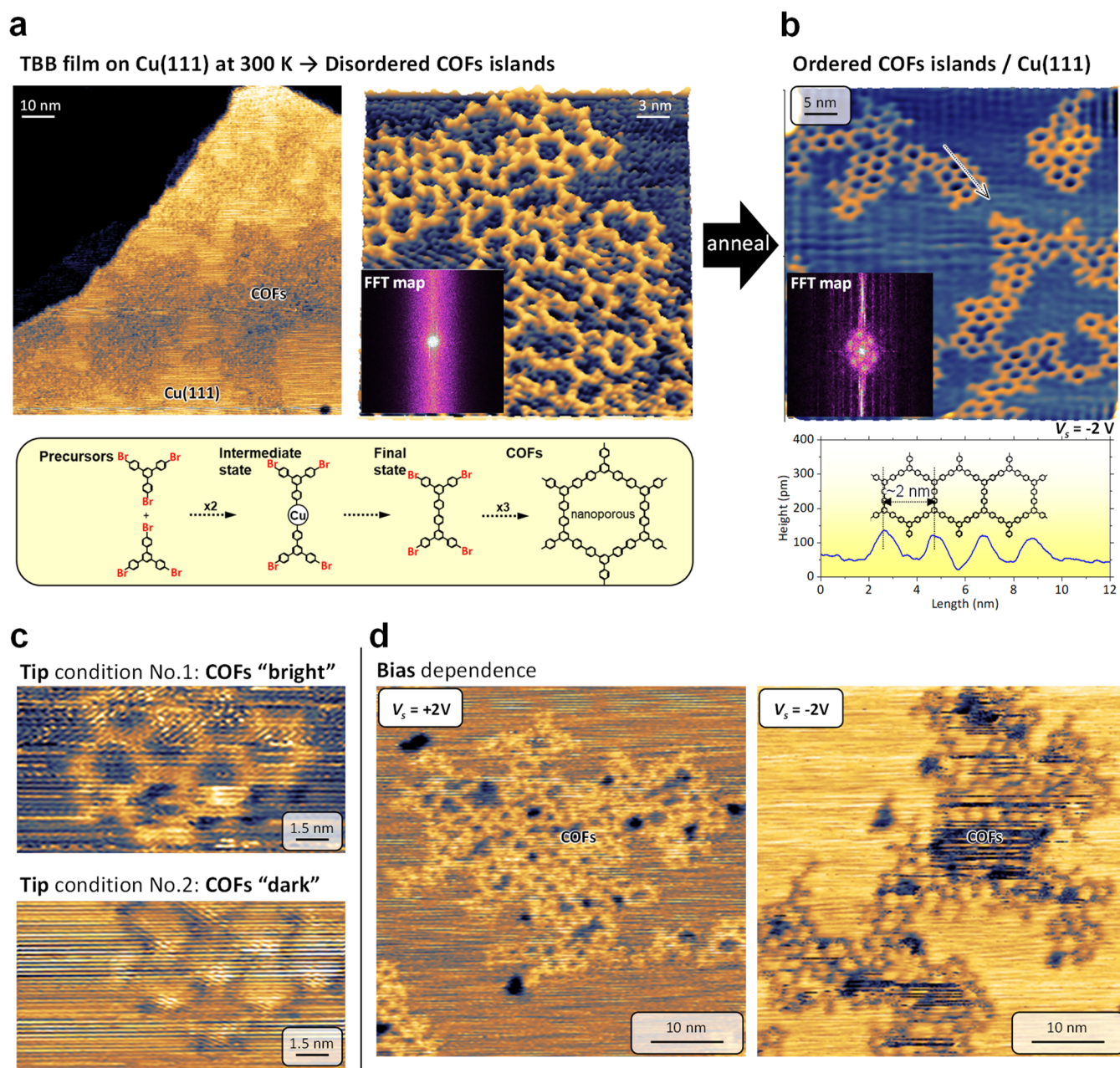


Figure 1. (a) UHV-STM topographic images obtained on the surface of TBB film grown on Cu(111) at 300 K (left panel: $100 \times 100 \text{ nm}^2$, $V_s = +2$ V, $I = 10$ pA; right panel: $30 \times 30 \text{ nm}^2$, $V_s = +2$ V, $I = 10$ pA). The lower panel denotes a honeycomb lattice formation model via the Ullmann reaction. The inset in the right panel denotes the FFT map, showing no symmetric spots. (b) STM topographic image of the ordered 2D-COFs islands on Cu(111) after the thermal annealing in UHV ($50 \times 50 \text{ nm}^2$, $V_s = -2$ V, $I = 443$ pA). The inset denotes the FFT map, representing broad hexagonal spots corresponding to the honeycomb symmetry. The lower panel denotes the height profile along the arrow in the topographic image, indicating the size of the nanopore. (c) STM topographic images of the same COFs obtained with different tip conditions (No. 1 and No. 2) ($15 \times 7.5 \text{ nm}^2$, $V_s = -2$ V, $I = 10$ pA). The former and the latter revealed the COFs as bright and dark lines, respectively. (d) Bias dependence in STM topographic images ($50 \times 50 \text{ nm}^2$, $I = 10$ pA). Left and right panels were taken at positive ($V_s = +2$ V) and negative ($V_s = -2$ V) bias voltages.

pristine Cu(111) substrate in ultrahigh vacuum (UHV) at room temperature. As our template, we employed a conventional 2D COF synthesized via on-surface synthesis through the Ullmann reaction,⁴³ using 1,3,5-tris(4-bromophenyl)benzene (TBB) precursors.^{20,44–49} This particular COF configuration offers nanopores of approximately 2 nm in size, with the capacity to accommodate approximately 60 Co atoms within its structure.

2. METHODS

2.1. Home-Built UHV STM Setup. A custom-built UHV-STM apparatus featuring analytical, preparation, and introduction chambers was employed for this study.^{50,51} Each chamber maintained a base pressure of approximately 10^{-8} Pa. The STM instrument was situated within the analytical chamber. We meticulously cleaned the STM tips, sample surfaces, and film formations in the preparation chamber. Transferring the cleaned STM tip and prepared samples was performed without breaking the UHV, so the cleaned tip and

sample were set into the STM. STM measurements were conducted at 300 K in UHV using a combined Nanonis SPM controller and software. The topographic images were acquired in a constant current mode, and the data obtained from the STM measurements were subsequently analyzed using WSxM 5.0 Develop 10.0 software.⁵²

2.2. UHV ARUPS/XPS/LEED Setup. ARUPS, XPS, and LEED measurements were performed in the custom-built UHV apparatus. All ARUPS and XPS measurements were executed at room temperature, using an ultralow-background, high-sensitivity ARUPS apparatus with a hemispherical electron energy analyzer (MBS A-1) and two monochromators (MBS M-1) for two wavelength regions as setup.^{53,54} He-I α ($h\nu = 21.218$ eV) and He-II α ($h\nu = 40.814$ eV) radiation sources were performed by a high-density plasma lamp (MBS L-1) with an Al filter. XPS was measured by irradiating X-ray (1486.6 eV) on the sample surface in the same UHV chamber. Doniach–Sunjic function was used for fitting the XPS data to determine peak positions. LEED with a multichannel plate (MCP) equipped in the preparation chamber was used to detect weak electron signals from the monolayer molecular film. A beam energy ranging from 10 to 50 eV was employed to minimize potential damage to the deposited molecular film. The sample current during LEED measurements remained below 100 nA.

2.3. Fabrication of STM Tips. STM tips were fabricated from polycrystalline W (purity 99.95%), Mo (purity 99.95%), and Pt₈₀Ir₂₀ wires with a diameter of 0.3 mm. This fabrication process involved both electrochemical etching⁵⁵ and flame-etching techniques.^{50,56} Subsequently, the prepared tips were carefully transferred into the UHV preparation chamber.

The tip apex underwent a thermal treatment, subjected to a temperature of 2000 K in UHV to eliminate any oxide layers on the apex of tungsten and molybdenum tips.⁵⁵ Following this cleaning procedure, the prepared and pristine tip was installed into the STM stage within the UHV analytical chamber.

2.4. Cu(111) Substrate Preparations. Our experiments employed two Cu(111) single crystals, each serving distinct purposes—one for ARUPS/XPS/LEED measurements and the other for STM.^{53,54,57,58} Both Cu(111) single crystals, having a diameter of 6 mm (MatecK, purity 99.9999%), underwent a meticulous process of sputtering and annealing to achieve clean and atomically flat surfaces in the preparation chambers ($<5.0 \times 10^{-8}$ Pa) (as detailed in the [Supporting Information](#), Figure S1).

The cleaning treatment for the Cu(111) single crystals involved Ar⁺ sputtering (+1.0 keV, 400 nA) with subsequent annealing (~ 820 K) utilizing electron bombardment⁵⁵ for the STM setup, and Ar⁺ sputtering (+0.6 keV, 3000 nA), followed by annealing (~ 800 K) using the infrared heater for the ARUPS setup.

2.5. On-Surface Synthesis of 2D COFs. The precursor employed in this study was 1,3,5-tris(4-bromophenyl)benzene (TBB, Tokyo Chemical Industry Co., Ltd., CAS RN: 7511-49-1, purity >98%) (Figure S4). TBB molecules, in the form of white powder, were placed within the alumina crucible of our custom-built molecular evaporator.⁵⁹ The crucible's temperature was raised through irradiation by the surrounding tungsten (W) filament loops. A type K thermocouple, in contact with the bottom of the crucible, closely monitored the crucible's temperature. We maintained the crucible temperature at approximately 390 K (filament power: 1.32 W = 1.10 A \times 1.20 V). This setup resulted in a sublimation rate of 0.155

nm/min, which we accurately monitored using a quartz crystal microbalance (QCM) with parameters z impedance = 1 and density = 1.⁵⁹

In this study, approximately 0.8 nm of TBB precursors, ascertained via QCM analysis, was deposited on both Au(001) and Cu(111) substrates. On the Au(001) substrate, the deposition of this 0.8 nm layer yielded a self-assembled monolayer (SAM) film at 300 K (Figure S2). Consequently, in the scope of this study, it can be posited that a 0.8 nm deposition is adequate to envelop the entire surface with a monolayer of TBB precursors.

Nevertheless, when we undertook the deposition of 0.8 nm of TBB molecules on Cu(111), only approximately 30% of the surface exhibited the formation of ordered COFs. This was attributed to the Ullmann reaction occurring at 300 K, which led to the formation of disordered COFs, attributed to the existence of an intermediate state (see Figure 1a). It is noteworthy, however, that the intermediate state evolved into the final state upon thermal annealing at approximately 430 K for a duration of 20 min in UHV⁶⁰ (as detailed in Figures 1 and S5). XPS measurements disclosed the presence of Br peaks at 182 eV (3p_{3/2}) and 190 eV (3p_{1/2})⁶¹ (refer to Figure 3b), indicating the persistence of residual Br atoms on the surface even following the annealing process.

2.6. Cobalt Deposition in UHV. Cobalt (Co) deposition was performed using two distinct evaporators: the AEV-3 evaporator from AVC Co., Ltd., integrated with the STM setup, and the EMF3/4 evaporator manufactured by Omicron. These depositions were conducted at a sample temperature of 300 K,^{54,62} as depicted in Figure S3. The same deposition rate was employed for both setups, amounting to 2.8 monolayers per minute (with a flux of 5.0 nA). To ensure precise quantification of the deposited Co, the deposition quantities were additionally calibrated through STM topographic images depicting the growth of Co islands on Cu(111), as displayed in Figure S3.

3. RESULTS AND DISCUSSION

The proliferation of two-dimensional covalent organic frameworks (2D COFs) on noble metallic substrates has undergone extensive scrutiny in recent decades. This exploration has unveiled the potential of inert surfaces, such as gold (Au) or silver (Ag), to catalyze the formation of 2D COFs through the adsorption of precursor molecules at ambient conditions, followed by annealing in an ultrahigh-vacuum (UHV) environment, employing the Ullmann reaction as the pivotal synthetic route.^{44,48}

The Ullmann reaction mechanism governing this hexagonal lattice structure may be elucidated by referencing the model presented in the lower panel in Figure 1a. The precursor, comprising a single TBB molecule, is characterized by a central benzene ring connected to three peripheral benzene rings, exhibiting C₃ symmetry, with bromine (Br) atoms capping its termini. After thermal annealing atop the noble metallic substrate, the desorption of Br atoms transpires. Concurrently, thermal diffusion augments the probability of precursor encounters, thereby facilitating the formation of novel covalent linkages between precursor molecules. The iterative execution of the Ullmann reaction culminates in the generation of 2D COFs.

Our initial investigation entailed the examination of TBB precursors' adsorption onto a meticulously prepared, atomically flat Au(001) surface, conducted in UHV at 300 K. This

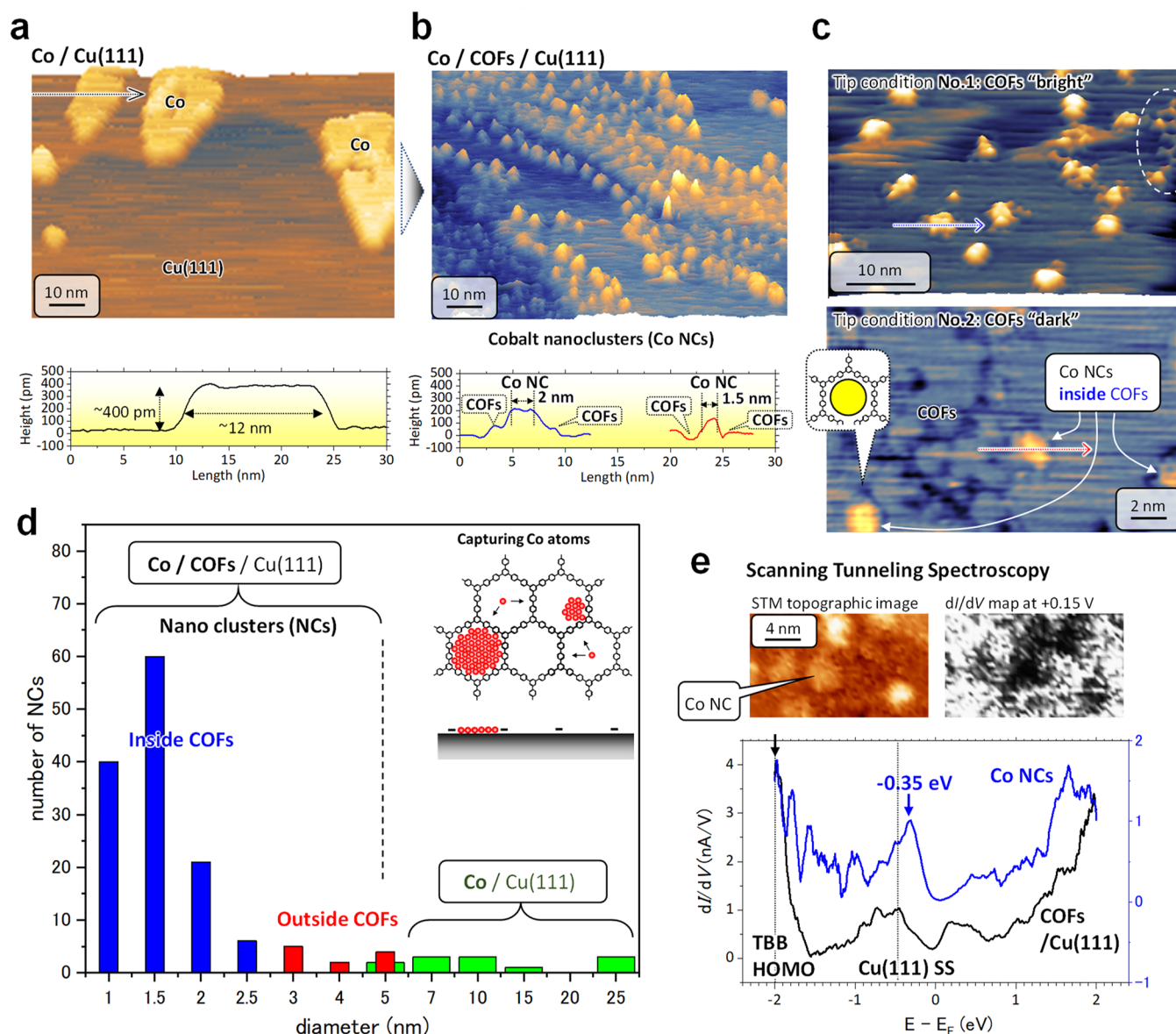


Figure 2. (a) UHV-STM topographic image obtained on the surface of triangular-shape bilayer Co islands grown on Cu(111) at 300 K ($100 \times 70 \text{ nm}^2$, $V_s = -1 \text{ V}$, $I = 50 \text{ pA}$). The lower panel denotes the height profile along the arrow. (b) UHV-STM topographic image of the COFs/Cu(111) surface after the Co deposition at 300 K ($100 \times 70 \text{ nm}^2$, $V_s = +2 \text{ V}$, $I = 52 \text{ pA}$). The lower panel denotes the height profiles along the blue and red arrows in (c). (c) Magnified STM topographic images. Upper panel: COFs appear as bright lines using the tip condition No. 1 ($50 \times 32 \text{ nm}^2$, $V_s = -2 \text{ V}$, $I = 41 \text{ pA}$). Lower panel: COFs appear as dark lines using the tip condition No. 2, in which the Co nanoclusters (Co NCs) inside the COFs are sharply visible and distinguished from COFs ($20 \times 13 \text{ nm}^2$, $V_s = +2 \text{ V}$, $I = 100 \text{ pA}$). (d) Histogram of different size Co NCs. Blue, red, and green bars denote the number of Co NCs grown inside COFs, outside COFs, and bare Cu(111), respectively. The inset denotes the NC formation model inside COFs. (e) Scanning tunneling spectroscopy (STS) results obtained on the Co NCs. The upper panels show an STM topographic image ($20 \times 12 \text{ nm}^2$, $V_s = -2 \text{ V}$, $I = 1 \text{ nA}$) and simultaneously obtained dI/dV map at +0.15 V. The lower panel represents dI/dV curves proportional to the sample LDOS. Blue and black lines were measured on the Co NCs and COFs/Cu(111), respectively. Dashed lines and arrows denote the Co surface state peak at -0.35 eV , TBB HOMO, and Cu(111) surface state (SS) peak around -0.45 eV .

procedure resulted in the establishment of a self-assembled monolayer (SAM) film, as depicted in Figure S2a,b. Subsequent thermal annealing in UHV induced the desorption of Br atoms from the precursors, thereby fostering covalent interactions among the precursor molecules. Consequently, this process facilitated the formation of 2D COFs on the surface, as elucidated in Figure S2c.

The primary objective of our investigation in this study is to leverage 2D COFs as a nanoporous honeycomb template for the growth of transition-metal nanoclusters (NCs). The realization of magnetic NCs necessitates the fulfillment of

two critical prerequisites: (1) the prevention of intercalation of adsorbed transition-metal atoms beneath the COFs, which could yield a monolayer film beneath the COFs, as opposed to the intended NCs, and (2) the avoidance of chemical bonding between the adsorbed transition-metal atoms and the COFs, as such interactions could jeopardize the structural integrity and regularity of the COFs.

To assess the capacity of 2D COFs in capturing transition-metal atoms, we conducted a comparative analysis of two distinct systems: one devoid of COFs and the other featuring the presence of COFs.

For the former system, we selected Co NCs on a Cu(111) substrate, a system well-documented for forming triangular-shaped bilayer NC islands with sizes ranging between 10 and 20 nm upon depositing approximately 0.2 monolayers (MLs) of Co at 300 K in UHV,^{54,62,63} as demonstrated in Figure S3.

Another rationale for selecting Cu(111) as our substrate lies in its capacity to prevent intermixing or interdiffusion between the adsorbed transition metals and noble-metal substrates.⁶⁴ This stems from the fact that Cu boasts a higher surface energy of 1850 mJ/m², compared to the surface energies of Au (1550 mJ/m²) and Ag (1250 mJ/m²).⁶⁵ It is worth noting that inert Au or Ag surfaces may exhibit weaker interactions with the 2D COFs, potentially leading to the unintended formation of a monolayer film beneath the COFs through intercalation.

Our initial step involved the meticulous preparation of a Cu(111) surface characterized by atomic flatness and cleanliness (>100 nm terrace width) in UHV (Figure S1). The verification of the substrate's morphology was executed through the utilization of scanning tunneling microscopy (STM), low-energy electron diffraction (LEED) analysis, which revealed 6-fold fcc(111) symmetry, and angle-resolved ultraviolet photoelectron spectroscopy (UPS), affirming the presence of the parabolic Shockley surface state, in agreement with previous studies.^{66,67}

Figure 1a shows STM topographic images acquired after introducing TBB precursors at 300 K in UHV onto the Cu(111) surface. On the Cu(111) atomic terrace, a discernible contrast between brighter and darker regions becomes evident, denoting the coexistence of two distinct materials on the surface, even at the relatively modest temperature of 300 K. This stands in marked contrast to the formation of the SAM on the Au surface (cf. Figure S2).

The magnified view presented in the right panel of Figure 1a reveals the formation of a network structure, suggesting that the Ullmann reaction has already transpired at 300 K on the Cu surface. However, the ordered nature of this network remains elusive, as the FFT map exhibits an absence of symmetric spots. This irregularity may be attributed to the intermediate state formation resulting from the Ullmann reaction,^{44,48} particularly the creation of C–Cu–C bonds between TBB precursors, which includes a copper atom, as illustrated in the lower panel of Figure 1a. Notably, numerous scratch lines are observable on the TBB/Cu surface within Figure 1a, potentially indicating the diffusion of desorbed Br atoms from the TBB precursors across the surface. This phenomenon could impede the further development of COFs, as the presence of Br atoms might constrain additional TBB adsorption on the surface. This observation is substantiated by XPS, which detected the residual Br atoms on this surface, as depicted in Figure 3 (we discuss later).

The energetically precarious intermediate state depicted in Figure 1a wholly transformed into the energetically favorable final state following annealing to 430 K (20 min) in UHV. This annealing process facilitated the formation of a honeycomb nanopore array through the establishment of covalent bonds among the precursor molecules. The STM topographic image in Figure 1b vividly illustrates the emergence of the 2D COFs. The FFT map reveals the presence of 6-fold spots, indicative of the ordered structure. A height profile along the arrow crossing three COFs nanopores, as depicted in the lower panel of Figure 1b, yields an approximate dimension of about 2 nm.

An additional intriguing facet worthy of mention pertains to the inherent instability observed during STM imaging of these

COFs on Cu(111) at 300 K in UHV when employing conventional PtIr and W metal tips. This instability may be attributed to the presence of residual Br atoms on the surface, which could adhere to the tip apex, thereby inducing alterations in the contrast within the STM images. Figure 1c illustrates this phenomenon. In the upper panel, the image portrays the COFs as bright lines, while, upon repeated scanning of the same region with the same tip, the appearance of the same COFs undergoes a transformation, as evidenced in the lower panel of Figure 1c, where the COFs are depicted as dark lines.

Furthermore, it is noteworthy that a contrast inversion was also detected upon altering the bias voltage, as exemplified in Figure 1d. Under identical tip conditions, the COFs were observed as bright lines at a bias voltage (V_s) = +2 V (left panel in Figure 1d), while they appeared as dark lines when the bias voltage was set to V_s = -2 V (right panel in Figure 1d).

While the visualization of the COFs does indeed hinge on the condition of the tip and the applied bias voltage, it is essential to highlight that these variables can be judiciously utilized to discern the positions of Co adsorption within the COFs region.

In assessing the efficacy of 2D COFs as trapping agents for generating transition-metal NCs, we undertook a comparative examination of submonolayer growth processes involving Co on Cu(111) and Co/COFs/Cu(111). As an initial step, approximately 0.2 monolayers (MLs) of Co was deposited on Cu(111) at 300 K in UHV (Figure 2a). During this process, the adsorbed Co atoms diffused thermally across the surface, culminating in the formation of triangular-shaped bilayer nanoislands, characterized by dimensions of 10–20 nm. This observation is corroborated by the height profile along the path traversing one such nanoisland, which reveals a height of approximately 400 pm and a width of roughly 12 nm.

Next, we deposited an equivalent quantity of Co onto the COFs/Cu(111) substrate at 300 K in UHV. Figures 2a and 2b have been presented at identical dimensions to clarify the nanocluster size. As illustrated in Figure 2b, the introduction of COFs engendered a marked transformation in the system, resulting in a reduction in the size of the NCs and a heightened proliferation of clusters. The height profiles, as displayed in the lower panel in Figure 2b and traversing two different NCs (as indicated by the blue and red arrows in Figure 2c), disclose a dimension of approximately 1.5–2.0 nm, aligning with the dimensions of the nanopores within the COFs, as previously observed in Figure 1b. These profiles were obtained using tip conditions No. 1 and No. 2. The tip conditions No. 1 and No. 2 appeared in the COFs as bright and dark lines (Figure 1d), which could resolve the Co and COFs positions. Moreover, the height measurement approximates around half (~200 pm) of the bilayer Co NC on Cu(111), as illustrated in Figure 2b, suggesting a monolayer configuration of cobalt within the Co NCs encapsulated within the COFs. The empirical evidence compellingly establishes the COFs on Cu(111) as proficient in entrapping Co atoms within their nanopores. The magnified images in Figure 2c provide a glimpse into cluster growth's progression.

It is discernible that a significant portion of the Co NCs is sequestered by the COFs islands, which effectively conceal the underlying COFs, thereby impeding a clear observation of the COFs' morphology. Nonetheless, within the area demarcated by the dotted circle in Figure 2c, we are able to discern the

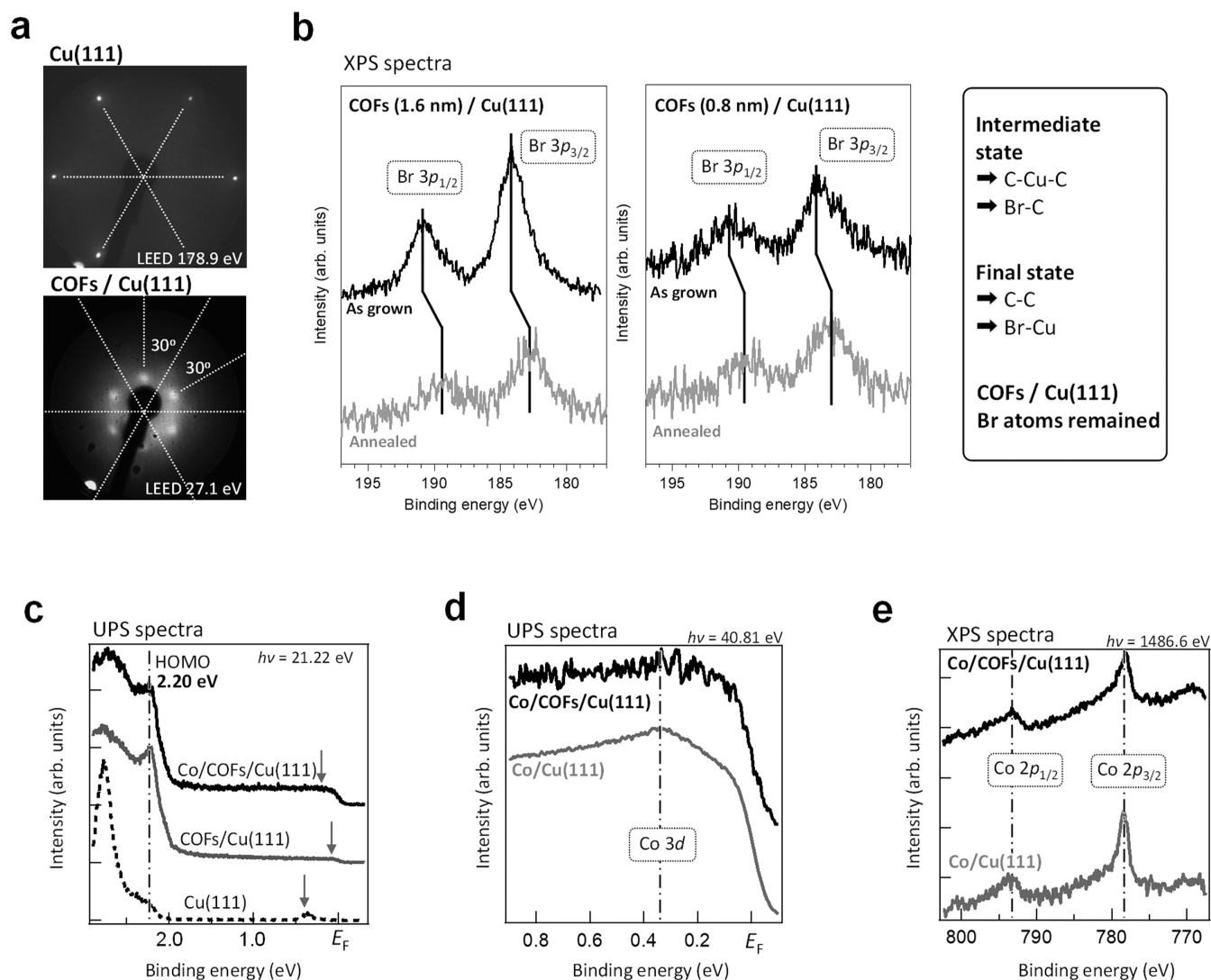


Figure 3. UHV-LEED, UPS, and XPS results. (a) LEED images obtained from the clean Cu(111) substrate at the electron beam energy of 178.9 eV (top panel) and COFs/Cu(111) at the beam energy of 27.1 eV (bottom panel). (b) XPS spectra for the Br 3p peaks obtained at the nominal molecular thicknesses of 1.6 nm (left panel) and 0.8 nm (right panel). For each thickness, the spectra for “as grown” (black) and “annealed” (gray) samples are shown. The vertical lines are shown to indicate the approximate positions of each of the peaks. The intermediate state before the annealing includes C–Cu–C and Br–C bonding, but the final state consists of C–C covalent and Br–Cu bonding. After the annealing in UHV, Br atoms remained on the surface. (c) UPS spectra for the Cu(111) (dotted line), COFs/Cu(111) (gray line), and Co/COFs/Cu(111) (black line). The dashed line marks the COFs flat HOMO position (2.20 eV). Arrows denote the Cu(111) surface states, in-gap state of COFs, and Co 3d surface states. (d) UPS spectra in the vicinity of the Fermi energy obtained on the Co/Cu(111) surface (gray line) and the Co/COFs/Cu(111) surface (black line). (e) XPS results around Co 2p orbitals obtained on the Co/Cu(111) surface (gray line) and the Co/COFs/Cu(111) surface (black line).

unaltered COFs, an observation that carries a pivotal implication.

As initially posited, it remains imperative to ensure that the COFs do not engage in chemical bonding with the adsorbed Co atoms, which might otherwise lead to the production of Co NCs and potentially culminate in the decomposition of the COFs. In this context, the outcome in the upper panel of Figure 2c serves as compelling evidence affirming the robustness of the COFs, specifically in terms of covalent bonding, in withstanding the demands of adsorption by active transition metals. This stands in stark contrast to the deposition of Co on SAM films, as reported previously.⁴⁰

Furthermore, within the delineated area encircled by the dotted circle, diminutive Co NCs were detected along the periphery of the COFs. This observation suggests the potential

initiation of NC growth commencing from the periphery, as opposed to the core of the nanopore.

Additional insights into the formation of the Co NC were gleaned through the utilization of a tip with contrast-reversible capabilities, as evidenced in Figures 1c and 1d. This specialized tip facilitated a clear differentiation between the COFs and the Co NC regions, with the COFs manifesting as dark lines in the lower panel of Figure 2c. The presence of these dark lines encircling each Co NC (indicated by bright dots) provides further evidence that the COFs’ nanopores effectively entrapped the Co atoms, fostering the in situ growth of NCs within these nanopores.

Crucially, it is noteworthy that this area in the lower panel of Figure 2c produced three distinct Co NCs while other COFs nanopores remained unoccupied. This observation suggests

that adsorbed Co atoms may be able to migrate or diffuse across the surface of the COFs yet come to a halt when they encounter a suitable Co nucleation site. It is imperative to emphasize that they might not intercalate beneath the COFs, an outcome indicative of stronger coupling between the π -orbitals of the COFs and the underlying Cu surface, thus serving as a constraint against Co intercalation beneath the COFs, as depicted in the inset models within Figure 2d.

In our quest for a comprehensive understanding of the size distribution of the formed Co NCs, we conducted a statistical analysis. Figure 2d encapsulates a complete summary, illustrating the quantity of Co NCs plotted against their respective diameters. A substantial majority of the Co clusters exhibit a size of approximately 1.5 nm, closely corresponding to the dimensions of the COFs' nanopores. This empirical finding serves as additional evidence substantiating Co atoms' confinement within the COFs' nanopores.

The inset model in Figure 2d proffers plausible mechanisms for forming Co NCs. As Co atoms adhere to the surface at 300 K, they can undergo thermal diffusion and migration across the nanopores. However, when these diffusing Co atoms become ensnared by the edges of the pores, instigating nucleation events, they serve as nuclei around which other thermally diffused Co atoms aggregate, ultimately culminating in the growth of a nanocluster.

Building upon the experimental findings illustrated in Figure 2c, it is reasonable to deduce that the electronic interaction between Co and the COFs should exhibit notable weakness. This hypothesis is directly affirmed through scanning tunneling spectroscopy (STS) measurements performed on this surface, as depicted in Figure 2e.

The simultaneous presentation of the topographic image and the differential conductance (dI/dV) map within Figure 2e effectively conveys the differentiation in the local density of states (LDOS) between Co NCs and the adjacent COFs on Cu(111). Notably, the former manifests an LDOS peak positioned at -0.35 eV (blue line in Figure 2e), while the latter exhibits some peaks within proximity of the Fermi energy, along with an additional peak around -2 eV.

Initially, the presence of the dI/dV curve obtained from the Co NCs within the COFs exhibited a peak at -0.35 eV. This substantiates the cobalt composition within the nanoclusters, as Co/Cu(111) is recognized for manifesting a spin-polarized peak at -0.35 eV.^{54,62,63} Subsequently, the dI/dV curve obtained on the COFs manifested several peaks near the Fermi energy. Because the well-known Cu(111) surface state (SS) peak is located at -0.45 eV, the observed peaks near -0.45 eV could potentially stem from the Cu(111) surface states penetrating the COFs' gap. Conversely, discernible LDOS peaks between $+0.2$ and $+0.4$ eV might represent in-gap states due to the formation of COFs. UPS findings in Figure 3c, marked by the arrow, also identified an escalated intensity around the Fermi energy on the COFs/Cu(111) compared to the pristine Cu(111), which is clearly visible in the ARUPS maps around 0 eV (= Fermi energy) in Figure S7.

In addition to the microscopic STM/STS measurements in Figures 1 and 2, LEED, UPS, and XPS measurements were further performed to understand macroscopic information, encompassing both the surface and interface regions. Figure 3a illustrates the LEED patterns obtained from the unaltered Cu(111) surface and the COFs/Cu(111) surface. The presence of distinct and well-defined six spots, aligning with the fcc-Cu(111) symmetry, characterizes the pristine Cu(111)

surface. However, following the thermal annealing of the TBB/Cu(111) surface, these sharp six spots vanish, signifying the comprehensive coverage of the surfaces by both the COFs and residual Br atoms. The appearance of broad, hexagonally symmetric LEED spots aligns with the ordered structure of the COFs on Cu(111) and is consistent with the 6-fold spots discernible in the fast Fourier transform (FFT) map in Figure 2b.

The XPS results pertaining to the Br $3p$ orbitals, as acquired during the deposition of TBB at two distinct thicknesses (0.8 and 1.6 nm) on Cu(111), both prior to and following thermal annealing, reveal the residual Br atoms, as depicted in Figure 3b. As a single nanopore within the COFs comprises 18 benzene rings (= 108 carbon atoms), achieved by excising 12 Br atoms from the TBB precursors using the Ullmann reaction (as depicted in the lower panel of Figure 1a), it can be inferred that Br atoms could cover approximately $\sim 11\%$ (= 12/108) of the surface, significantly below the coverage of a monolayer. Additionally, the intensity of the Br peak diminished subsequent to annealing (Figure 3b), suggesting a reduction in the quantity of Br atoms present on the surface during the annealing process. Although Br atoms are not visually apparent in the STM topographic images, as indicated in Figure 1c, we have previously noted frequent changes in the tip's behavior, which might suggest the incidental pickup of diffusing Br atoms on the Cu surface at a temperature of 300 K.

An intriguing feature is the peak shift of approximately 1.3 eV, which becomes evident when comparing the XPS spectra before and after annealing. This shift may be attributed to transitioning from the intermediate to the final state. In other words, it implies that a significant portion of the chemical bonding has transitioned from Br–C bonding involving the TBB precursors to Br–Cu bonding with the underlying copper surface.

The UPS spectra have disclosed the presence of a discernible highest occupied molecular orbital (HOMO) peak, positioned at 2.20 eV below the Fermi energy on COFs/Cu(111). Furthermore, an ARUPS map, presented in a second-derivative plot, showcases the flat dispersion of the HOMO in k -space, as depicted in Figures S6 and S7. Notably, the position of this HOMO peak remains unaltered both prior to and following the deposition of Co, as illustrated in Figure 3c. However, there is a noticeable increase in intensity at approximately 0.35 eV, as evidenced in Figures 3c and 3d, aligning with the -0.35 eV peak in the dI/dV curve from Figure 2e. This alignment suggests a correlation with the spin-polarized Co $3d$ surface state of Co/Cu(111).^{54,62} Furthermore, a meticulous examination of the Co $2p$ orbitals and the impact of Co adsorption was conducted. Nevertheless, the XPS outcomes revealed no clear distinctions between Co/Cu(111) (gray line) and Co/COFs (black line), as presented in Figure 3e. This implies that Co might not engage in electronic hybridization with the HOMO of the COFs. This finding aligns with prior XPS results obtained from Co NCs situated within metal–organic frameworks, which likewise failed to indicate any chemical bonding between cobalt and the carbon, nitrogen, and sulfur atoms within those systems.⁶⁸ We further checked that there was no significant shift of the carbon $1s$ peak of the COFs before and after the Co deposition (Figure S8), indicating weak electronic interactions between COFs and Co.

Consequently, we can assert that no clear electronic hybridization exists between the transition metal and the 2D COFs on Cu(111). This outcome can be attributed to the

pronounced covalent bonding within the COFs, which prevails over the interaction between the molecule and the transition metal's 3d orbitals. This covalent bonding enables the thermal diffusion of Co atoms to traverse through the COFs without undergoing significant electronic interaction with the COFs.

4. CONCLUSIONS

Our investigation has demonstrated that the 2D COFs prepared on Cu(111) exhibit a remarkable capability for entrapping Co NCs of equivalent size (~2 nm) within their nanopores. All STM/STS, UPS/XPS, and LEED measurements were conducted at a temperature of 300 K within a UHV environment.

This Co NC formation can be attributed to several key factors: (1) the absence of monolayer film growth below the COFs; (2) the preservation of COFs even after Co adsorption; (3) Co atoms can migrate or diffuse across the COFs until they are captured by nucleation sites located at the edges of the COFs; (4) the aggregation of other diffusing Co atoms at these nucleation sites results in larger NCs. However, the size of the NCs remains constrained by the dimensions of the COFs' nanopores.

These compelling experimental findings chart a novel path for producing Co NCs composed of dozens of atoms utilizing 2D COFs. This breakthrough holds immense promise across a myriad of application domains, including quantum dots, quantum bits, spintronics, biomedicine, drug delivery, catalysts, and water purification.

■ ASSOCIATED CONTENT

SI Supporting Information

The Supporting Information is available free of charge at <https://pubs.acs.org/doi/10.1021/acs.jpcc.3c07435>.

UHV-STM, LEED, and ARUPS results of the cleaned Cu(111) substrate; UHV-STM results of TBB SAM films on Au(001) and 2D COFs on Au(001); UHV-STM, UPS, and XPS results of cobalt deposition on Cu(111); precursor molecule deposition process on Cu(111) in UHV at 300 K; UHV-STM and LEED results obtained before and after the post-annealing of the TBB/Cu(111); angle-resolved UPS maps obtained on Cu(111) and COFs/Cu(111) before and after the post-annealing; angle-resolved UPS maps in a differential mode obtained on Cu(111) and COFs/Cu(111) before and after the post-annealing; XPS spectra for the C 1s and Co 2p peaks before and after the thermal annealing of TBB films and before and after the Co deposition on TBB/Cu(111) (PDF)

■ AUTHOR INFORMATION

Corresponding Author

Toyo Kazu Yamada – Department of Materials Science, Chiba University, Chiba 263-8522, Japan; Molecular Chirality Research Centre, Chiba University, Chiba 263-8522, Japan; orcid.org/0000-0001-5185-6472; Email: toyoyamada@faculty.chiba-u.jp

Authors

Shingo Kanazawa – Department of Materials Science, Chiba University, Chiba 263-8522, Japan; Institute for Molecular Science, Okazaki 444-8585, Japan

Keisuke Fukutani – Institute for Molecular Science, Okazaki 444-8585, Japan

Satoshi Kera – Institute for Molecular Science, Okazaki 444-8585, Japan; orcid.org/0000-0003-0353-5863

Complete contact information is available at:

<https://pubs.acs.org/10.1021/acs.jpcc.3c07435>

Notes

The authors declare no competing financial interest.

■ ACKNOWLEDGMENTS

This work was supported by JSPS KAKENHI Grants 17K19023, 23H02033, and 23H05461, the Murata Science Foundation, the Shorai Foundation for Science and Technology, TEPCO Memorial Foundation, Casio Science Promotion Foundation, and the Toshiaki Ogasawara Memorial Foundation. Shingo Kanazawa was supported by the Special Inter-University Researcher program organized by the Institute for Molecular Science. We thank Dr. Eiichi Inami for carefully reading our manuscript and fruitful discussions.

■ REFERENCES

- (1) Doonan, C. J.; Tranchemontagne, D. J.; Glover, T. G.; Hunt, J. R.; Yaghi, O. M. Exceptional Ammonia Uptake by a Covalent Organic Framework. *Nat. Chem.* **2010**, *2* (3), 235–238.
- (2) Furukawa, H.; Yaghi, O. M. Storage of Hydrogen, Methane, and Carbon Dioxide in Highly Porous Covalent Organic Frameworks for Clean Energy Applications. *J. Am. Chem. Soc.* **2009**, *131* (25), 8875–8883.
- (3) Zeng, Y.; Zou, R.; Zhao, Y. Covalent Organic Frameworks for CO₂ Capture. *Adv. Mater.* **2016**, *28* (15), 2855–2873.
- (4) Romero-Muñiz, I.; Mavrandonakis, A.; Albacete, P.; Vega, A.; Brioso, V.; Zamora, F.; Platero-Prats, A. E. Unveiling the Local Structure of Palladium Loaded into Imine-Linked Layered Covalent Organic Frameworks for Cross-Coupling Catalysis. *Angew. Chem., Int. Ed.* **2020**, *59* (31), 13013–13020.
- (5) Lin, S.; Diercks, C. S.; Zhang, Y.-B.; Kornienko, N.; Nichols, E. M.; Zhao, Y.; Paris, A. R.; Kim, D.; Yang, P.; Yaghi, O. M.; Chang, C. J. Covalent Organic Frameworks Comprising Cobalt Porphyrins for Catalytic CO₂ Reduction in Water. *Science* **2015**, *349* (6253), 1208–1213.
- (6) Xu, H.; Gao, J.; Jiang, D. Stable, Crystalline, Porous, Covalent Organic Frameworks as a Platform for Chiral Organocatalysts. *Nat. Chem.* **2015**, *7* (11), 905–912.
- (7) Ge, L.; Qiao, C.; Tang, Y.; Zhang, X.; Jiang, X. Light-Activated Hypoxia-Sensitive Covalent Organic Framework for Tandem-Responsive Drug Delivery. *Nano Lett.* **2021**, *21* (7), 3218–3224.
- (8) Zhang, L.; Wang, S.; Zhou, Y.; Wang, C.; Zhang, X.; Deng, H. Covalent Organic Frameworks as Favorable Constructs for Photodynamic Therapy. *Angew. Chem., Int. Ed.* **2019**, *58* (40), 14213–14218.
- (9) Li, M.; Qiao, S.; Zheng, Y.; Andaloussi, Y. H.; Li, X.; Zhang, Z.; Li, A.; Cheng, P.; Ma, S.; Chen, Y. Fabricating Covalent Organic Framework Capsules with Commodious Microenvironment for Enzymes. *J. Am. Chem. Soc.* **2020**, *142* (14), 6675–6681.
- (10) Zhang, P.; Chen, S.; Zhu, C.; Hou, L.; Xian, W.; Zuo, X.; Zhang, Q.; Zhang, L.; Ma, S.; Sun, Q. Covalent Organic Framework Nanofluidic Membrane as a Platform for Highly Sensitive Bionic Thermosensation. *Nat. Commun.* **2021**, *12* (1), 1844.
- (11) Guo, J.; Xu, Y.; Jin, S.; Chen, L.; Kaji, T.; Honsho, Y.; Addicoat, M. A.; Kim, J.; Saeki, A.; Ihee, H.; Seki, S.; Irle, S.; Hiramoto, M.; Gao, J.; Jiang, D. Conjugated Organic Framework with Three-Dimensionally Ordered Stable Structure and Delocalized π Clouds. *Nat. Commun.* **2013**, *4* (1), 2736.
- (12) Bessinger, D.; Ascherl, L.; Auras, F.; Bein, T. Spectrally Switchable Photodetection with Near-Infrared-Absorbing Covalent

- Organic Frameworks. *J. Am. Chem. Soc.* **2017**, *139* (34), 12035–12042.
- (13) Chen, H.; Tu, H.; Hu, C.; Liu, Y.; Dong, D.; Sun, Y.; Dai, Y.; Wang, S.; Qian, H.; Lin, Z.; Chen, L. Cationic Covalent Organic Framework Nanosheets for Fast Li-Ion Conduction. *J. Am. Chem. Soc.* **2018**, *140* (3), 896–899.
- (14) Shi, R.; Liu, L.; Lu, Y.; Wang, C.; Li, Y.; Li, L.; Yan, Z.; Chen, J. Nitrogen-Rich Covalent Organic Frameworks with Multiple Carbonyls for High-Performance Sodium Batteries. *Nat. Commun.* **2020**, *11* (1), 178.
- (15) Chen, Z.; Berger, R.; Müllen, K.; Narita, A. On-Surface Synthesis of Graphene Nanoribbons through Solution-Processing of Monomers. *Chem. Lett.* **2017**, *46* (10), 1476–1478.
- (16) Denawi, H.; Koudia, M.; Hayn, R.; Siri, O.; Abel, M. On-Surface Synthesis of Spin Crossover Polymeric Chains. *J. Phys. Chem. C* **2018**, *122* (26), 15033–15040.
- (17) Di Giovannantonio, M.; Eimre, K.; Yakutovich, A. V.; Chen, Q.; Mishra, S.; Urgel, J. I.; Pignedoli, C. A.; Ruffieux, P.; Müllen, K.; Narita, A.; Fasel, R. On-Surface Synthesis of Antiaromatic and Open-Shell Indeno[2,1-*b*]Fluorene Polymers and Their Lateral Fusion into Porous Ribbons. *J. Am. Chem. Soc.* **2019**, *141* (31), 12346–12354.
- (18) Dobner, C.; Li, G.; Sarker, M.; Sinitskii, A.; Enders, A. Diffusion-Controlled on-Surface Synthesis of Graphene Nanoribbon Heterojunctions. *RSC Adv.* **2022**, *12* (11), 6615–6618.
- (19) Fan, Q.; Martin-Jimenez, D.; Werner, S.; Ebeling, D.; Koehler, T.; Vollgraff, T.; Sundermeyer, J.; Hieringer, W.; Schirmeisen, A.; Gottfried, J. M. On-Surface Synthesis and Characterization of a Cycloarene: C108 Graphene Ring. *J. Am. Chem. Soc.* **2020**, *142* (2), 894–899.
- (20) Hao, Z.; Song, L.; Yan, C.; Zhang, H.; Ruan, Z.; Sun, S.; Lu, J.; Cai, J. On-Surface Synthesis of One-Type Pore Single-Crystal Porous Covalent Organic Frameworks. *Chem. Commun.* **2019**, *55* (72), 10800–10803.
- (21) Su, J.; Fan, W.; Mutombo, P.; Peng, X.; Song, S.; Ondráček, M.; Golub, P.; Brabec, J.; Veis, L.; Telychko, M.; Jelínek, P.; Wu, J.; Lu, J. On-Surface Synthesis and Characterization of [7]Triangulene Quantum Ring. *Nano Lett.* **2021**, *21* (1), 861–867.
- (22) Sun, K.; Silveira, O. J.; Ma, Y.; Hasegawa, Y.; Matsumoto, M.; Kera, S.; Krejčí, O.; Foster, A. S.; Kawai, S. On-Surface Synthesis of Disilabenzene-Bridged Covalent Organic Frameworks. *Nat. Chem.* **2023**, *15*, 136.
- (23) Urgel, J. I.; Bock, J.; Di Giovannantonio, M.; Ruffieux, P.; Pignedoli, C. A.; Kivala, M.; Fasel, R. On-Surface Synthesis of π -Conjugated Ladder-Type Polymers Comprising Nonbenzenoid Moieties. *RSC Adv.* **2021**, *11* (38), 23437–23441.
- (24) Virmani, E.; Rotter, J. M.; Mähringer, A.; von Zons, T.; Godt, A.; Bein, T.; Wuttke, S.; Medina, D. D. On-Surface Synthesis of Highly Oriented Thin Metal–Organic Framework Films through Vapor-Assisted Conversion. *J. Am. Chem. Soc.* **2018**, *140* (14), 4812–4819.
- (25) Yi, D. K.; Selvan, S. T.; Lee, S. S.; Papaefthymiou, G. C.; Kundaliya, D.; Ying, J. Y. Silica-Coated Nanocomposites of Magnetic Nanoparticles and Quantum Dots. *J. Am. Chem. Soc.* **2005**, *127* (14), 4990–4991.
- (26) Di Corato, R.; Bigall, N. C.; Ragusa, A.; Dorfs, D.; Genovese, A.; Marotta, R.; Manna, L.; Pellegrino, T. Multifunctional Nanobeads Based on Quantum Dots and Magnetic Nanoparticles: Synthesis and Cancer Cell Targeting and Sorting. *ACS Nano* **2011**, *5* (2), 1109–1121.
- (27) Tejada, J.; Chudnovsky, E. M.; Barco, E. D.; Hernandez, J. M.; Spiller, T. P. Magnetic Qubits as Hardware for Quantum Computers. *Nanotechnology* **2001**, *12* (2), 181–186.
- (28) Bertaina, S.; Gambarelli, S.; Mitra, T.; Tsukerblat, B.; Müller, A.; Barbara, B. Quantum Oscillations in a Molecular Magnet. *Nature* **2008**, *453* (7192), 203–206.
- (29) Singamaneni, S.; Bliznyuk, V. N.; Binek, C.; Tsymbal, E. Y. Magnetic Nanoparticles: Recent Advances in Synthesis, Self-Assembly and Applications. *J. Mater. Chem.* **2011**, *21* (42), 16819.
- (30) Wang, C.; Meyer, J.; Teichert, N.; Auge, A.; Rausch, E.; Balke, B.; Hütten, A.; Fecher, G. H.; Felser, C. Heusler Nanoparticles for Spintronics and Ferromagnetic Shape Memory Alloys. *J. Vac. Sci. Technol. B Nanotechnol. Microelectron. Mater. Process. Meas. Phenom.* **2014**, *32* (2), No. 020802.
- (31) Berry, C. C.; Curtis, A. S. G. Functionalisation of Magnetic Nanoparticles for Applications in Biomedicine. *J. Phys. Appl. Phys.* **2003**, *36* (13), R198–R206.
- (32) Pankhurst, Q. A.; Connolly, J.; Jones, S. K.; Dobson, J. Applications of Magnetic Nanoparticles in Biomedicine. *J. Phys. Appl. Phys.* **2003**, *36* (13), R167–R181.
- (33) Shubayev, V. I.; Pisanic, T. R.; Jin, S. Magnetic Nanoparticles for Theragnostics. *Adv. Drug Delivery Rev.* **2009**, *61* (6), 467–477.
- (34) Dobson, J. Magnetic Nanoparticles for Drug Delivery. *Drug Dev. Res.* **2006**, *67* (1), 55–60.
- (35) Govan, J.; Gun'ko, Y. Recent Advances in the Application of Magnetic Nanoparticles as a Support for Homogeneous Catalysts. *Nanomaterials* **2014**, *4* (2), 222–241.
- (36) Kainz, Q. M.; Reiser, O. Polymer- and Dendrimer-Coated Magnetic Nanoparticles as Versatile Supports for Catalysts, Scavengers, and Reagents. *Acc. Chem. Res.* **2014**, *47* (2), 667–677.
- (37) Abu-Reziq, R.; Alper, H.; Wang, D.; Post, M. L. Metal Supported on Dendronized Magnetic Nanoparticles: Highly Selective Hydroformylation Catalysts. *J. Am. Chem. Soc.* **2006**, *128* (15), 5279–5282.
- (38) Ambashta, R. D.; Sillanpää, M. Water Purification Using Magnetic Assistance: A Review. *J. Hazard. Mater.* **2010**, *180* (1–3), 38–49.
- (39) Inami, E.; Shimasaki, M.; Yorimitsu, H.; Yamada, T. K. Room Temperature Stable Film Formation of π -Conjugated Organic Molecules on 3d Magnetic Substrate. *Sci. Rep.* **2018**, *8* (1), 353.
- (40) Inami, E.; Yamaguchi, M.; Nemoto, R.; Yorimitsu, H.; Krüger, P.; Yamada, T. K. Direct Imaging of Precursor Adcomplex States during Cryogenic-Temperature On-Surface Metalation: Scanning Tunneling Microscopy Study on Porphyrin Array with Fe Adsorption at 78.5 K. *J. Phys. Chem. C* **2020**, *124* (6), 3621–3631.
- (41) Gottfried, J. M. Surface Chemistry of Porphyrins and Phthalocyanines. *Surf. Sci. Rep.* **2015**, *70* (3), 259–379.
- (42) Yamada, T. K.; Yamagishi, Y.; Nakashima, S.; Kitaoka, Y.; Nakamura, K. Role of π -d Hybridization in a 300-K Organic-Magnetic Interface: Metal-Free Phthalocyanine Single Molecules on a Bcc Fe(001) Whisker. *Phys. Rev. B* **2016**, *94* (19), No. 195437.
- (43) Ullmann, F.; Bielecki, J. Ueber Synthesen in Der Biphenylreihe. *Berichte Dtsch. Chem. Ges.* **1901**, *34* (2), 2174–2185.
- (44) Gutzler, R.; Walch, H.; Eder, G.; Kloft, S.; Heckl, W. M.; Lackinger, M. Surface Mediated Synthesis of 2D Covalent Organic Frameworks: 1,3,5-Tris(4-Bromophenyl)Benzene on Graphite(001), Cu(111), and Ag(110). *Chem. Commun.* **2009**, No. 29, 4456.
- (45) Furukawa, H.; Ko, N.; Go, Y. B.; Aratani, N.; Choi, S. B.; Choi, E.; Yazaydin, A. Ö.; Snurr, R. Q.; O'Keeffe, M.; Kim, J.; Yaghi, O. M. Ultrahigh Porosity in Metal-Organic Frameworks. *Science* **2010**, *329* (5990), 424–428.
- (46) Peyrot, D.; Silly, F. On-Surface Synthesis of Two-Dimensional Covalent Organic Structures versus Halogen-Bonded Self-Assembly: Competing Formation of Organic Nanoarchitectures. *ACS Nano* **2016**, *10* (5), 5490–5498.
- (47) Larrea, C. R.; Baddeley, C. J. Fabrication of a High-Quality, Porous, Surface-Confined Covalent Organic Framework on a Reactive Metal Surface. *ChemPhysChem* **2016**, *17* (7), 971–975.
- (48) Doyle, C. M.; McGuinness, C.; Lawless, A. P.; Preobrajenski, A. B.; Vinogradov, N. A.; Cafolla, A. A. Surface Mediated Synthesis of 2D Covalent Organic Networks: 1,3,5-Tris(4-bromophenyl)Benzene on Au(111). *Phys. Status Solidi B* **2019**, *256* (2), No. 1800349.
- (49) Dong, L.; Liu, P. N.; Lin, N. Surface-Activated Coupling Reactions Confined on a Surface. *Acc. Chem. Res.* **2015**, *48* (10), 2765–2774.
- (50) Goto, Y.; Suizu, R.; Noguchi, Y.; Yamada, T. K. Oxidative Vaporization Etching for Molybdenum Tip Formation in Air. *Appl. Surf. Sci.* **2021**, *542*, No. 148642.

- (51) Goto, Y.; Ando, S.; Kakugawa, K.; Takahara, S.; Yamada, T. K. Unzipping Process of Wet Carbon Nanotubes Adsorbed on Cu(111) in Ultra-High Vacuum: an STM/STS study. *Vac. Surf. Sci.* **2021**, *64* (1), 40–46.
- (52) Horcas, I.; Fernández, R.; Gómez-Rodríguez, J. M.; Colchero, J.; Gómez-Herrero, J.; Baro, A. M. WSXM: A Software for Scanning Probe Microscopy and a Tool for Nanotechnology. *Rev. Sci. Instrum.* **2007**, *78* (1), No. 013705.
- (53) Nemoto, R.; Krüger, P.; Putri Hartini, A. N.; Hosokai, T.; Horie, M.; Kera, S.; Yamada, T. K. Well-Ordered Monolayer Growth of Crown-Ether Ring Molecules on Cu(111) in Ultra-High Vacuum: An STM, UPS, and DFT Study. *J. Phys. Chem. C* **2019**, *123* (31), 18939–18950.
- (54) Nemoto, R.; Krüger, P.; Hosokai, T.; Horie, M.; Kera, S.; Yamada, T. K. Room-Temperature Deposition of Cobalt Monolayer on (7 × 4) Crown-Ether Ring Molecular Array: Ultra-High Vacuum STM and UPS Study. *Vac. Surf. Sci.* **2020**, *63* (9), 465–469.
- (55) Yamada, T. K.; Abe, T.; Nazriq, N. M. K.; Irisawa, T. Electron-Bombarded <110>-Oriented Tungsten Tips for Stable Tunneling Electron Emission. *Rev. Sci. Instrum.* **2016**, *87* (3), No. 033703.
- (56) Yamaguchi, T.; Inami, E.; Goto, Y.; Sakai, Y.; Sasaki, S.; Ohno, T.; Yamada, T. K. Fabrication of Tungsten Tip Probes within 3 s by Using Flame Etching. *Rev. Sci. Instrum.* **2019**, *90* (6), No. 063701.
- (57) Nazriq, N. K. M.; Krüger, P.; Yamada, T. K. Carbon Monoxide Stripe Motion Driven by Correlated Lateral Hopping in a 1.4 × 1.4 Monolayer Phase on Cu(111). *J. Phys. Chem. Lett.* **2020**, *11* (5), 1753–1761.
- (58) Nazriq, N. K. M.; Minamitani, E.; Yamada, T. K. CO-Tip Manipulation Using Repulsive Interactions. *Nanotechnology* **2018**, *29* (49), No. 495701.
- (59) Inami, E.; Yamaguchi, M.; Yamaguchi, T.; Shimasaki, M.; Yamada, T. K. Controlled Deposition Number of Organic Molecules Using Quartz Crystal Microbalance Evaluated by Scanning Tunneling Microscopy Single-Molecule-Counting. *Anal. Chem.* **2018**, *90* (15), 8954–8959.
- (60) Eichhorn, J.; Nieckarz, D.; Ochs, O.; Samanta, D.; Schmittel, M.; Szabelski, P. J.; Lackinger, M. On-Surface Ullmann Coupling: The Influence of Kinetic Reaction Parameters on the Morphology and Quality of Covalent Networks. *ACS Nano* **2014**, *8* (8), 7880–7889.
- (61) Chen, M.; Xiao, J.; Steinrück, H.-P.; Wang, S.; Wang, W.; Lin, N.; Hieringer, W.; Gottfried, J. M. Combined Photoemission and Scanning Tunneling Microscopy Study of the Surface-Assisted Ullmann Coupling Reaction. *J. Phys. Chem. C* **2014**, *118* (13), 6820–6830.
- (62) Schmaus, S.; Bagrets, A.; Nahas, Y.; Yamada, T. K.; Bork, A.; Bowen, M.; Beaupaire, E.; Evers, F.; Wulffhekel, W. Giant Magnetoresistance through a Single Molecule. *Nat. Nanotechnol.* **2011**, *6* (3), 185–189.
- (63) Pietzsch, O.; Okatov, S.; Kubetzka, A.; Bode, M.; Heinze, S.; Lichtenstein, A.; Wiesendanger, R. Spin-Resolved Electronic Structure of Nanoscale Cobalt Islands on Cu(111). *Phys. Rev. Lett.* **2006**, *96* (23), No. 237203.
- (64) Bischoff, M. M. J.; Yamada, T. K.; van Kempen, H. Analysis of the Short-Range Order of the Au/Fe(001) Surface Alloy. *Phys. Rev. B* **2003**, *67* (16), No. 165403.
- (65) Miedema, A. R.; de Châtel, P. F.; de Boer, F. R. Cohesion in Alloys — Fundamentals of a Semi-Empirical Model. *Phys. BC* **1980**, *100* (1), 1–28.
- (66) Hörmandinger, G. Imaging of the Cu(111) Surface State in Scanning Tunneling Microscopy. *Phys. Rev. B* **1994**, *49* (19), 13897–13905.
- (67) Olsson, F. E.; Persson, M.; Borisov, A. G.; Gauyacq, J.-P.; Lagoute, J.; Fölsch, S. Localization of the Cu(111) Surface State by Single Cu Adatoms. *Phys. Rev. Lett.* **2004**, *93* (20), No. 206803.
- (68) Ge, X.; Di, H.; Wang, P.; Miao, X.; Zhang, P.; Wang, H.; Ma, J.; Yin, L. Metal–Organic Framework-Derived Nitrogen-Doped Cobalt Nanocluster Inlaid Porous Carbon as High-Efficiency Catalyst for Advanced Potassium–Sulfur Batteries. *ACS Nano* **2020**, *14* (11), 16022–16035.